IRIS AperTO

UNIVERSITÀ DEGLI STUDI DI TORINO

AperTO - Archivio Istituzionale Open Access dell'Università di Torino

Thermal behaviour of siliceous faujasite: Further structural interpretation of negative thermal expansion

This is the author's manuscript

Original Citation:

Availability:

This version is available http://hdl.handle.net/2318/154478 since 2018-06-12T10:13:50Z

Published version:

DOI:10.1016/j.micromeso.2014.10.006

Terms of use:

Open Access

Anyone can freely access the full text of works made available as "Open Access". Works made available under a Creative Commons license can be used according to the terms and conditions of said license. Use of all other works requires consent of the right holder (author or publisher) if not exempted from copyright protection by the applicable law.

(Article begins on next page)

12 October 2024

This Accepted Author Manuscript (AAM) is copyrighted and published by Elsevier. It is posted here by agreement between Elsevier and the University of Turin. Changes resulting from the publishing process - such as editing, corrections, structural formatting, and other quality control mechanisms - may not be reflected in this version of the text. The definitive version of the text was subsequently published in MICROPOROUS AND MESOPOROUS MATERIALS, 202, 2015, 10.1016/j.micromeso.2014.10.006.

You may download, copy and otherwise use the AAM for non-commercial purposes provided that your license is limited by the following restrictions:

(1) You may use this AAM for non-commercial purposes only under the terms of the CC-BY-NC-ND license.

(2) The integrity of the work and identification of the author, copyright owner, and publisher must be preserved in any copy.

(3) You must attribute this AAM in the following format: Creative Commons BY-NC-ND license (http://creativecommons.org/licenses/by-nc-nd/4.0/deed.en), 10.1016/j.micromeso.2014.10.006

The publisher's version is available at:
http://linkinghub.elsevier.com/retrieve/pii/S1387181114005800

When citing, please refer to the published version.

Link to this full text:
http://hdl.handle.net/2318/154478

This full text was downloaded from iris - AperTO: https://iris.unito.it/

iris - AperTO

University of Turin's Institutional Research Information System and Open Access Institutional Repository

Thermal behaviour of siliceous faujasite: Further structural interpretation of negative thermal expansion

Lara Leardini, Simona Quartieri, Giovanna Vezzalini, Rossella Arletti

Abstract

The high-temperature behaviour of siliceous faujasite (Si-Y) was investigated by in situ synchrotron X-ray powder diffraction from room temperature up to 1123 K. This porous phase is remarkably stable when heated, and no phase transitions or changes in symmetry are observed. A marked negative thermal expansion (NTE), already reported in literature for a heating range from 25 to 573 K, was confirmed up to about 923 K. Above this temperature a positive thermal expansion was observed. Si-Y's thermal behaviour was interpreted on the basis of the transverse thermal vibrations of the oxygen atoms involved in the T–O–T linkages and a series of other structural features characterizing the faujasite structure, namely the T–T distances between adjacent tetrahedral sites, the thickness of the double 6-membered rings, and the ditrigonal index of the 6-membered rings. Moreover, the thermal behaviour of several other anhydrous porous materials with NTE behaviour is discussed and compared to that of Si-Y.

Graphical abstract

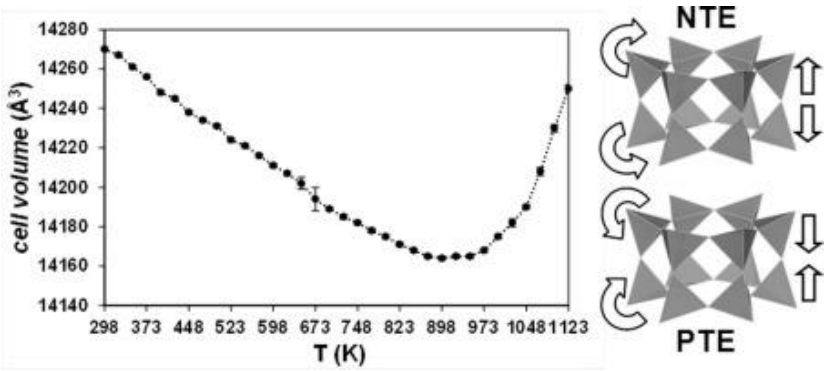

Keywords

- Siliceous faujasite;
- Thermal behaviour;
- NTE;
- In situ time-resolved X-ray powder diffraction;
- Rietveld refinement

1. Introduction

Knowledge of the thermal coefficient of a particular zeolite is of paramount importance for many applications, including prediction of possible mechanical issues for the supported polycrystalline zeolitic membranes. In particular, understanding the mechanisms governing heat-induced structural deformations is crucial for many materials used, for example, in aerospace technologies, microchips, optical devices, etc. [1] and [2].

In general, solid materials expand when heated, *i.e.* they exhibit positive coefficients of thermal expansion (PTE). A minority of solids exhibit a negative thermal expansion (NTE) (see *i.e.* [3], [4] and [5]), which means contraction upon heating. The NTE generally arises from supramolecular structural mechanisms,

which can be ascribed to high order effects, such as ferroelectric, magnetostrictive and displacive phase transitions, or low frequency phonon modes [6], the presence of rigid unit modes (RUMs) [7], and librations.

The majority of structures exhibiting NTE share a common feature: the presence of oxygen atoms involved in M–O–M or Si–O–Si linkages. These linkages are typical of complex metal oxides [8] and [9], metal cyanides [10], polymers [11], and zeolites (see *i.e.* [12], [13], [14], [15], [16], [17], [18] and [19]). The mechanisms governing NTE in these materials are summarized by Sleight [3]. In particular, in open frameworks, the main mechanism is the presence of transverse thermal vibrations of the oxygen atoms in M–O–M linkages. These motions may occur cooperatively in open framework structures, where rigid MOx polyhedra are hinged by two-coordinated oxygen atoms. Relatively large void space volumes, compared to the framework volumes, are required to accommodate the cooperative rotations of polyhedra. Since the positive thermal expansion of strong metal–oxygen bonds within the MOx polyhedra is negligible, the polyhedra are free to rotate as rigid units with little or no internal distortions. This latter mechanism has been rationalized theoretically on the basis of the so-called rigid unit mode (RUM) model [7]. RUMs are low-frequency lattice vibration modes with very low or zero energy cost and are readily excited. The increase in vibrational amplitude of RUMs as a function of temperature is thus regarded as the underlying mechanism for the origin of NTE in framework structures ([20] and references therein).

It is well known that, when heated, zeolites may undergo different kinds of structural changes including: (i) cell volume contraction due to the removal of water and/or templating organic molecules; (ii) displacive or reconstructive phase transformations to more or less metastable phases; (iii) breaking (and new formation) of T–O–T bonds; (iv) structural breakdown; and (v) negative thermal expansion in the dehydrated phases [21].

Tschaufeser and Parker [22] applied lattice dynamics to calculate the thermal expansion coefficients from 0 to 500 K of 18 siliceous and non-siliceous zeolites. All the investigated porous materials showed a significant cell volume contraction, except sodalite and cancrinite. The authors underlined that these two phases were, of all the materials studied, the most dense and the only ones with a one-dimensional channel system. Lightfoot [17] reviewed the thermal behaviour of 17 experimentally studied microporous solids (calcined siliceous zeolites, AlPO and MAPO; Table 2 in [17]). Only two materials, CIT-5 and $AlPO_4$-31 (again dense materials with a one-dimensional channel system), showed an overall volume expansion. Based upon the results of this work, the authors suggested that NTE is the norm rather than the exception for zeolites, even if a framework structure possessing rigid units seems to be necessary, but not sufficient in itself, for NTE behaviour to occur.

More recently, Cruciani [21] reviewed the NTE behaviour of the dehydrated forms of several zeolites and zeotypes. A few examples occur among natural zeolites (e.g. wairakite [21] and analcime [23]) whereas the list of synthetic zeolites − most of them in their pure silica form and in the following labelled with their framework type [24] − is considerably larger: MFI [14], [25], [26], [27], [28], [29], [30], [31], [32] and [33]; ERI ($AlPO_4$-17) [15]; AEI ($ALPO_4$-18) [34]; zeolite A [35] and [36]; RHO [37], [38] and [39]; MWW, ITE, IFR and STT [12]; CHA and IFR [13], [18], [34] and [40]; ISV and STF [17]; FER [19], SOD (Si-SOD) [41]; FAU (Na-X) [31], [42] and [43] and FAU (Si-Y) [16] and [44].

In the specific case of faujasite, a marked NTE was experimentally observed for siliceous faujasite (hereinafter Si-Y) [16], and for SAPO-37 with a faujasite-type structure [44]. Attfield and Sleight [16] attributed the NTE behaviour to the transverse vibrations of the Si–O–Si bridging oxygen atoms − a mode of lattice vibration that is of low enough energy to be excited even at low temperatures − and to the coupled rotations of the tetrahedra. Buragadda et al. [44] analysed the results obtained for SAPO-37 and concluded that the substitution of Si by Al and P has essentially no effect on the thermal expansion properties of these FAU-type materials. In fact, although the two materials were investigated in two different T ranges (303–773 K and 25–573 K, for SAPO-37 and Si-Y, respectively), the overall thermal expansion coefficients calculated in the same intermediate T-range 303–573 K are very similar ($\alpha_{V(303–573\ K)} = -12.2 \times 10^{-6}\ K^{-1}$ and $-11.5 \times 10^{-6}\ K^{-1}$, for Si-Y and SAPO-37, respectively).

Concerning Na-X, Couvest et al. [42] observed NTE from 25 K to room temperature (rT), while at higher T (423–723 K) Noack et al. [31] reported a positive thermal expansion. Further lattice dynamics simulation studies performed on Na-X by [43] confirmed these behaviours.

The above mentioned results on FAU phases reveal that, at present, the investigated T ranges are rather heterogeneous and in general are limited to about 700 K. Moreover, limited detailed structural data are exploited to interpret the T-induced deformations. In the present work, the high-temperature (HT) behaviour of Si-Y was investigated by in situ synchrotron X-ray powder diffraction from rT to 1123 K, with the following aims: (i) to describe the response of this material to heating in a much wider T range than those previously reported, and (ii) to provide a more detailed structural interpretation of the deformations undergone under HT by this porous phase.

2. Experimental

2.1. Materials

The faujasite sample used in this work ($H^{+}_{1.90}[Al_{1.90}Si_{190.10}O_{384}]$, s.g. *Fd*-3*m*, *a* = 24.259(4), [45]) was purchased from the Tosoh Corporation. The framework structure of the Si-Y zeolite (FAU-type framework topology [24]) is obtained when the cuboctahedral sodalite cages (or β-cages) $[4^6 6^8]$ are linked together at four of the eight 6-ring windows by double hexagonal rings (D6Rs) (Fig. 1). The resulting structure is characterized by large cavities referred to as “supercages” or “α-cages”, with a diameter of approximately 12 Å, interconnected via 12 membered-ring (12MR) windows (7.4 Å free diameter) to four other supercages. The topological symmetry is cubic *Fd*-3*m*, which corresponds to a fully disordered Si/Al distribution.

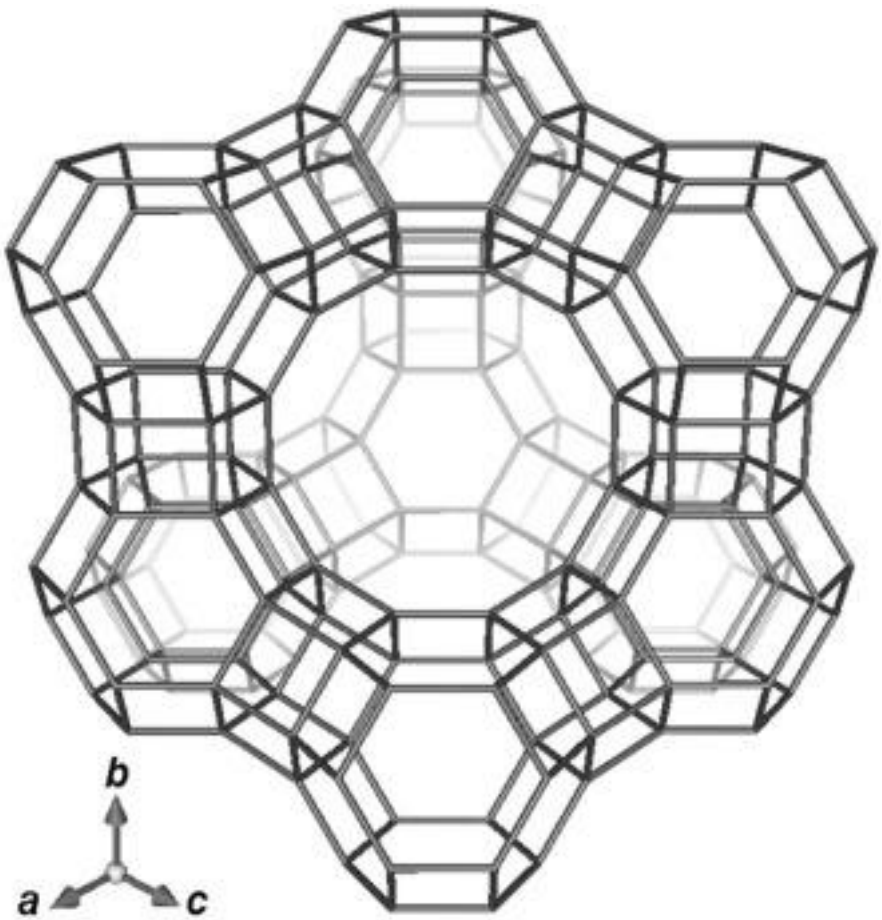

Fig. 1. Perspective view of the faujasite framework along the [1 1 1] direction. Structure figure was prepared by the VESTA software [58].

2.2. Thermogravimetric analysis (TGA)

TGA analysis was performed using a Seiko SSC 5200 thermal analyzer. The powder sample (11.698 mg) was loaded in a Pt crucible and heated from rT to 1123 K under a constant flux of air, at a heating rate of 5 K/min.

2.3. Synchrotron radiation X-ray powder diffraction experiments

The time-resolved X-ray powder diffraction experiments (SR-XRPD) were performed at the MCX beamline of the Elettra Synchrotron Light Source (Trieste – Italy). The powdered sample of Si-Y was carefully packed inside a 0.5 mm quartz capillary open at both ends. Data were acquired in parallel Debye–Scherrer geometry, with a wavelength of 0.8278 Å; the rotating capillary sample was heated in situ using a furnace from rT up to 1123 K with a heating rate of 5 K/min. The wavelength was calibrated using Si as external standard, while temperature calibration was achieved by measuring the thermal expansion of platinum [46] collected under the same experimental conditions. During the heating process, the diffraction patterns were collected every 25 K on a translating image plate detector and then integrated into one-dimensional powder patterns with the FIT2D software [47]. Selected integrated powder patterns as a function of temperature are shown in Fig. 2.

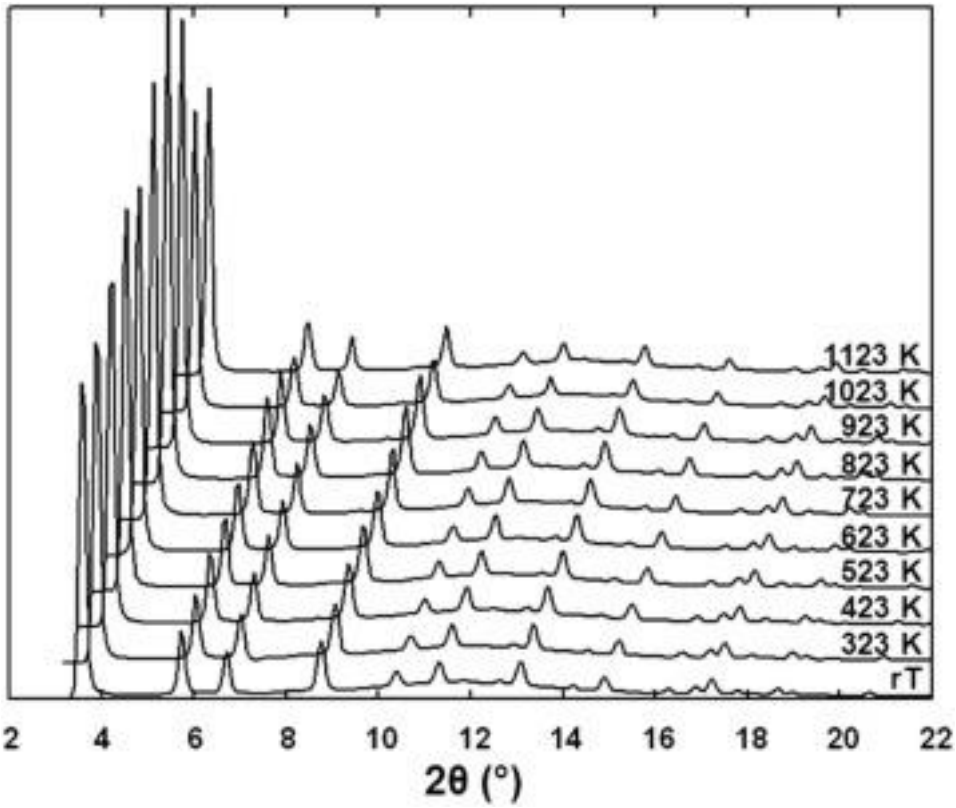

Fig. 2. Selected powder patterns of Si-Y as a function of temperature.

2.4. Structural refinements

The evolution of the structural features as a function of temperature was followed by full profile Rietveld refinements. Structural refinements were carried out using the GSAS computer program [48], with the EXPGUI interface [49], in the *Fd*-3*m* space group starting from the atomic positions reported by Braschi et al. [45] for the same sample. Since no evidence was found to support a change in symmetry in the powder patterns until 1123 K, the cubic *Fd*-3*m* space group was used in all the structure refinements.

The extracted Bragg peak profiles were modelled by a pseudo-Voigt function [50] with 5 refined coefficients (three Gaussian and two Lorentzian terms: Gu, Gv, Gw, Lx, and Ly in GSAS terminology) and a 0.01% peak

intensity cut-off. The instrumental background was empirically fitted with a 24 refined coefficient Chebyshev polynomial of the first order. The 2θ-zero shift, scale factor and unit-cell parameters were accurately refined in all the patterns of the data set. The refined structural parameters for each data histogram were fractional coordinates and isotropic displacement factors of the framework atoms. Soft-constraints were applied to the T–O distances (1.60 Å) with tolerance values (σ) of 0.04 Å. Isotropic thermal displacement factors were constrained to be the same for each type of atom.

Si-Y final observed and calculated powder patterns at rT, 523 K, 723 K, 923 K, and 1123 K are shown in the Supplementary Material (Fig. 1S). For the same selected temperatures, lattice parameters and refinement details are reported in Table 1; atomic coordinates are reported in the Supplementary Material (Table 1S); T–O bond distances and T–T distances (Å) together with O–T–O and T–O–T angles (°) in Table 2; the dimensions of the double-six ring (D6R), 6-membered ring of the sodalite cage ($6MR_{sod}$), and 12-membered ring (12MR) in Table 3. The unit cell parameters up to 1123 K are provided as Supplementary Material (Table 2S).

Table 1. Unit-cell parameters and details of the structural refinements at selected temperatures.

	rT	**523 K**	**723 K**	**923 K**	**1123 K**
Space group	*Fd-3m*	*Fd-3m*	*Fd-3m*	*Fd-3m*	*Fd-3m*
a (Å)	24.256(1)	24.229(1)	24.207(1)	24.195(1)	24.244(2)
V (Å^3)	14,270(1)	14,224(1)	14,185(1)	14,165(1)	14,250(2)
2θ range (°)	2.8–58.4	2.8–58.4	2.8–58.4	2.8–58.4	2.8–58.4
R_{wp} (%)	6.32	6.42	6.67	6.54	6.82
R_p (%)	4.34	4.41	4.41	4.30	5.14
R_F^2 (%)	9.96	9.27	8.83	9.94	13.43
N_o of reflections	628	624	622	622	624
N_{obs}	1012	1012	1012	1012	1012
N_{var}	44	44	44	44	44

λ = 0.8278 Å.

$$R_p = \sum[Y_{io} - Y_{ic}]/\sum Y_{io};\ R_{wp} = [\sum w_i(Y_{io} - Y_{ic})^2/\sum w_i Y_{io}^2]^{0.5};\ R_F2 = \sum|F_o^2 - F_c^2|/\sum|F_o^2|$$

Table 2. Bond distances (Å) and angles (°) within the Si-Y framework at room temperature (rT), 523, 723, 923 and 1123 K from in situ time-resolved data.

	rT	**523 K**	**723 K**	**923 K**	**1123 K**
Tetrahedral bond distances (Å)					
T1–O1	1.612(6)	1.606(7)	1.604(7)	1.603(7)	1.603(5)
T1–O2	1.609(6)	1.601(6)	1.600(7)	1.603(7)	1.601(5)
T1–O3	1.600(6)	1.594(6)	1.595(6)	1.590(6)	1.596(5)
T1–O4	1.608(6)	1.609(7)	1.608(7)	1.600(7)	1.599(5)
<T–O>	1.607(6)	1.603(7)	1.602(7)	1.599(7)	1.600(5)
<T–O>corr	1.612(6)	1.608(7)	1.609(7)	1.608(7)	1.612(5)
O–T–O bond angles (°)					
O1–T1–O2	110.4(9)	110.3(9)	110.8(10)	110.5(11)	110.0(12)
O1–T1–O3	107.7(13)	107.9(13)	108.5(14)	109.8(15)	107.8(18)
O1–T1–O4	108.0(8)	108.5(8)	108.5(9)	109.1(9)	109.9(8)

	rT	523 K	723 K	923 K	1123 K
O2–T1–O3	108.9(11)	110.6(12)	108.7(12)	110.0(13)	108.7(13)
O2–T1–O4	108.3(13)	107.3(12)	107.6(13)	106.8(13)	108.4(16)
O3–T1–O4	113.5(13)	112.2(14)	112.8(15)	110.7(16)	112.1(17)
<O–T–O>	110(1)	109(1)	110(1)	110(1)	109(1)
T–O–T bond angles (°)					
T–O1–T	140(2)	139(2)	139(2)	138(2)	142(2)
T–O2–T	150(1)	150(2)	151(2)	151(2)	154(2)
T–O3–T	147(2)	149(2)	148(2)	150(2)	152(2)
T–O4–T	139(2)	140(2)	140(2)	141(2)	138(2)
<T–O–T>	144(1)	145(2)	145(2)	145(2)	147(2)
T–T distances (Å)					
T–T (O1)	3.03(1)	3.01(1)	3.00(2)	2.99(2)	3.03(2)
T–T (O2)	3.11(1)	3.09(1)	3.10(2)	3.10(2)	3.12(2)
T–T (O3)	3.07(1)	3.07(1)	3.07(2)	3.07(2)	3.10(1)
T–T (O4)	3.01(2)	3.03(2)	3.02(2)	3.02(2)	2.98(2)
<T–T>	3.05(1)	3.05(1)	3.05(2)	3.05(2)	3.06(2)

 <T–O>corr = mean tetrahedral bond distance corrected for thermal motion following the Simple Rigid Body (SRB) model [51].

Table 3. Dimensions of the double-six ring (D6R), the 6-membered ring of the sodalite cage ($6MR_{sod}$) and of the 12-membered ring (12MR) at room temperature (rT), 523, 723, 923 and 1123 K from in situ time-resolved data.

	rT	523 K	723 K	923 K	1123 K
Double-six ring (D6R) thickness					
O4–O4 (Å)	5.03(2)	5.05(2)	5.04(3)	5.06(3)	5.05(3)
O4–O1–O4 (°)	149(1)	150(2)	151(2)	152(2)	149(2)
6-membered ring of the D6R ($6MR_{D6R}$) dimensions					
O2–O3 (Å)	5.07(3)	5.13(3)	5.08(3)	5.13(3)	5.12(3)
O2–O2 (Å)	4.92(4)	4.96(4)	4.89(4)	4.91(4)	4.83(5)
O3-O3 (Å)	3.86(3)	3.91(3)	3.90(3)	3.96(3)	4.04(4)
$I_{d\ D6R}$	1.27(2)	1.27(2)	1.25(2)	1.24(2)	1.20(3)
6-membered ring of the sodalite cage ($6MR_{sod}$) dimensions					
O2–O4 (Å)	5.05(2)	5.02(3)	5.02(3)	5.00(3)	5.03(4)
O2–O2 (Å)	3.85(3)	3.85(3)	3.86(4)	3.87(4)	3.92(4)
O4–O4 (Å)	4.85(4)	4.80(4)	4.77(4)	4.74(4)	4.72(5)
$I_{d\ 6R}$	1.26(2)	1.25(2)	1.24(2)	1.22(2)	1.20(2)
12-membered ring (12MR) dimensions					
O1–O1 (Å)	9.87(4)	9.84(4)	9.88(5)	9.79(4)	9.88(5)
O4–O4 (Å)	9.87(4)	9.90(4)	9.82(4)	9.92(5)	9.86(5)
E	1.000(8)	1.005(8)	1.005(9)	1.013(9)	1.00(1)

I_{dD6R} = O2-O2/O3-O3; $I_{d\ 6R}$ = O4-O4/O2-O2; *E* = ratio between the largest and smallest O–O diameters.

3. Results

3.1. Temperature-dependent variations of unit cell parameters

As can be seen in the powder patterns of Fig. 2, Si-Y is remarkably stable upon heating, and no phase transitions or changes in symmetry are observed during the experiment. Up to 873–923 K the diffraction peaks shift slightly towards higher 2θ values, while above this temperature the shift occurs in the opposite direction.

Fig. 3 reports the values for *a* axis and cell volume as a function of temperature. Two opposite trends are clearly visible below and above 923 K. In particular, below 923 K, the *a* parameter slightly decreases ($\Delta a = -0.25\%$, $\alpha a = -4.02 \times 10^{-6}$ K^{-1}) with a consequent negative volume expansion ($\Delta V = -0.74\%$; $\alpha_V = -11.77 \times 10^{-6}$ K^{-1}). In the same T range, the TG curve (Fig. 4) shows a minor weight loss (−1.72 wt%). Considering the weight loss due to residual humidity below 373 K (−1.18 wt%), only a very slight weight loss can be attributed to the removal of structural water molecules (−0.54 wt%, corresponding to about 4 H_2O/u.c.). Since the rate of the unit-cell volume contraction in the 373–923 K T-range ($\Delta V/\Delta T\% = -16.55$) is much faster than that of the weight loss (Δweight/$\Delta T\% = -0.10$), the effect of this small water content on the Si-Y thermal behaviour can be considered negligible. These results confirm a negative thermal expansion effect for Si-Y, as already reported in literature [16], although only up to 573 K. Above 923 K, the *a*-axis starts to lengthen and, as a result, a positive volume expansion is registered ($\Delta V_{923–1123\ K} = +0.60\%$; $\alpha_V = +30.00 \times 10^{-6}$ K^{-1}, $\Delta a_{923–1123\ K} = +0.20\%$; $\alpha a = +10.00 \times 10^{-6}$ K^{-1}). This process continues up to the highest investigated temperature (1123 K), but without complete recovery of the rT values. In the same T-range (923–1123 K), no significant weight loss is registered in the TG curve (Fig. 4), thus confirming the positive thermal expansion behaviour at high temperature, which, as far as the authors are aware, has never been discussed for Si-Y in literature.

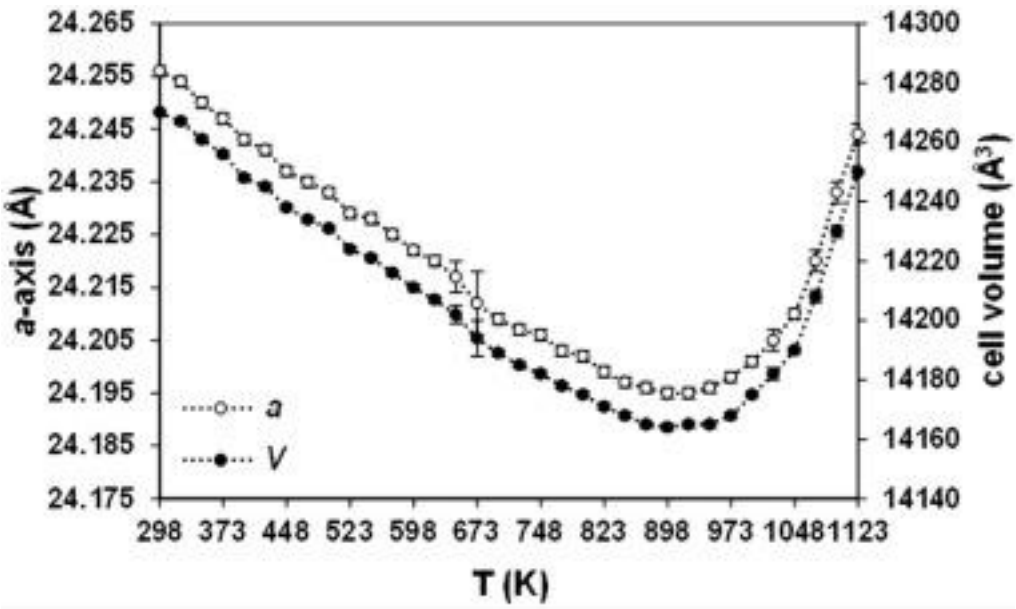

Fig. 3. Unit cell parameters of Si-Y as a function of temperature.

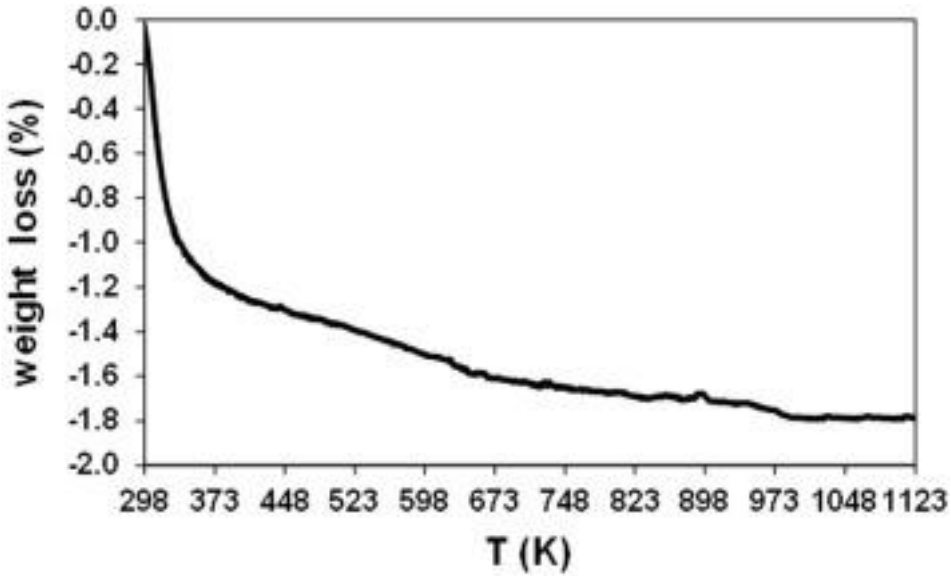

Fig. 4. TG curve of Si-Y.

3.2. Temperature-dependent structural modifications

Notwithstanding the small absolute variations of cell parameters, and the rather high error bars, with increasing T (Table 2 and Table 3) a change in the T-evolution of some structural features was observed passing from the NTE to the PTE regime. Hence, a structural interpretation of the thermal behaviour of Si-Y was attempted.

Table 2 and Fig. 2S illustrate the evolution of the mean T–O bond distance (<T–O>) as a function of temperature, first without and then after correcting for the thermal motion, following the Simple Rigid Body (SRB) model [51]. In both cases, a very slight change in the slope of the T-evolution is observed corresponding with the NTE/PTE boundary; however, considering the error bars of the data, these changes cannot be considered significant in the overall T range. At the same time, the O–T–O bond angles also remain substantially unchanged (Table 2), thus making it reasonable to consider the TO_4 tetrahedra as rigid bodies.

Also concerning the mean T–O–T angle (<T–O–T>) and the mean T–T distance (<T–T>), no relevant variations can be discerned in the whole investigated T range, even if a perceptible slope increase is observed above 923 K (Fig. 5a and b and Table 2). This evidence suggested the need to select some specific bond distances and angles to obtain a more detailed description of Si-Y thermal induced deformation. To this aim, the most meaningful parameter was found to be the distance between the two tetrahedral sites connected by the O1 oxygen atom (hereinafter T–T(O1) distance), which decreases up to 923 K and inverts its trend in the PTE regime (Fig. 6 and Table 2). The shortening of T–T(O1) can be attributed to the transverse vibrations of the bridging oxygen atom O1, readily excited at low temperatures [16]. Conversely, the T–T(O1) lengthening in the PTE region can be ascribed to the longitudinal vibrations, which dominate at higher temperatures. These variations in T–T(O1) are accompanied by an appreciable slope change in the evolution of the T–O1–T angle (Fig. 6 and Table 2). Overall, the trend shown by T–T(O1) (Fig. 6) recalls that of the cell parameters (Fig. 3), and considering that the O1 “hinge” is the bridging oxygen atom between the two six-rings of the D6R, it is thus evident that the main structural changes undergone by Si-Y involve the D6R units. More specifically, in the NTE regime, the shortening in the T–T(O1) distance is accompanied by a decrease in the T–O1–T angle and by an increase in the corresponding O4–O1–O4 inter-tetrahedral angle. As a result, the O4–O4 distance (corresponding to the D6R thickness) slightly increases through a cooperative anti-rotation of the tetrahedra around the O1 oxygen (Fig. 6c). Above 923 K, in the PTE regime, the slope of the T-dependence curve of the abovementioned parameters inverts and, in particular, the D6R thickness decreases (Fig. 6d).

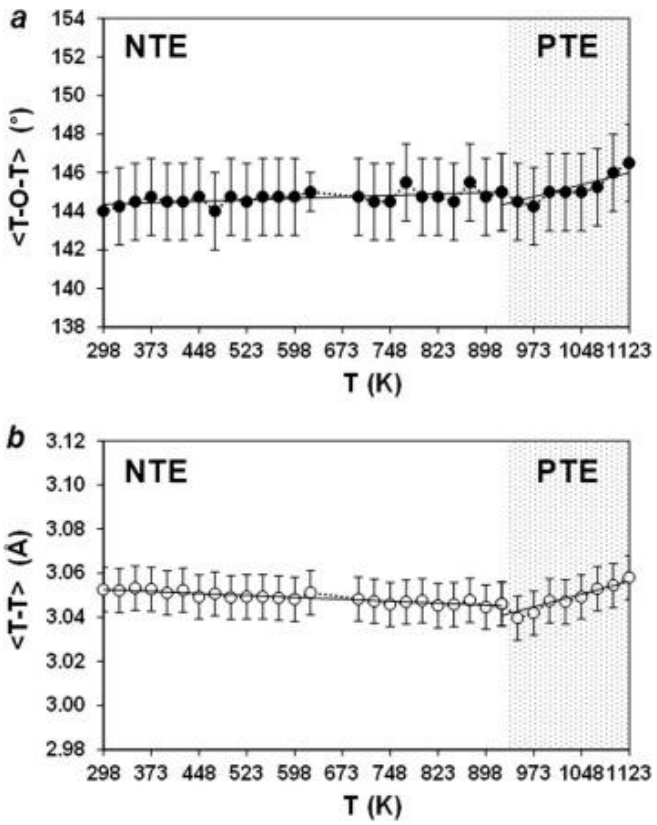

Fig. 5. Mean T–O–T bond angle (<T–O–T>) and mean T–T distance (<T–T>) as a function of temperature. In the plot, the two thermal behaviour regimes NTE and PTE are shown. In the figure, a black dotted background indicates the PTE temperature range.

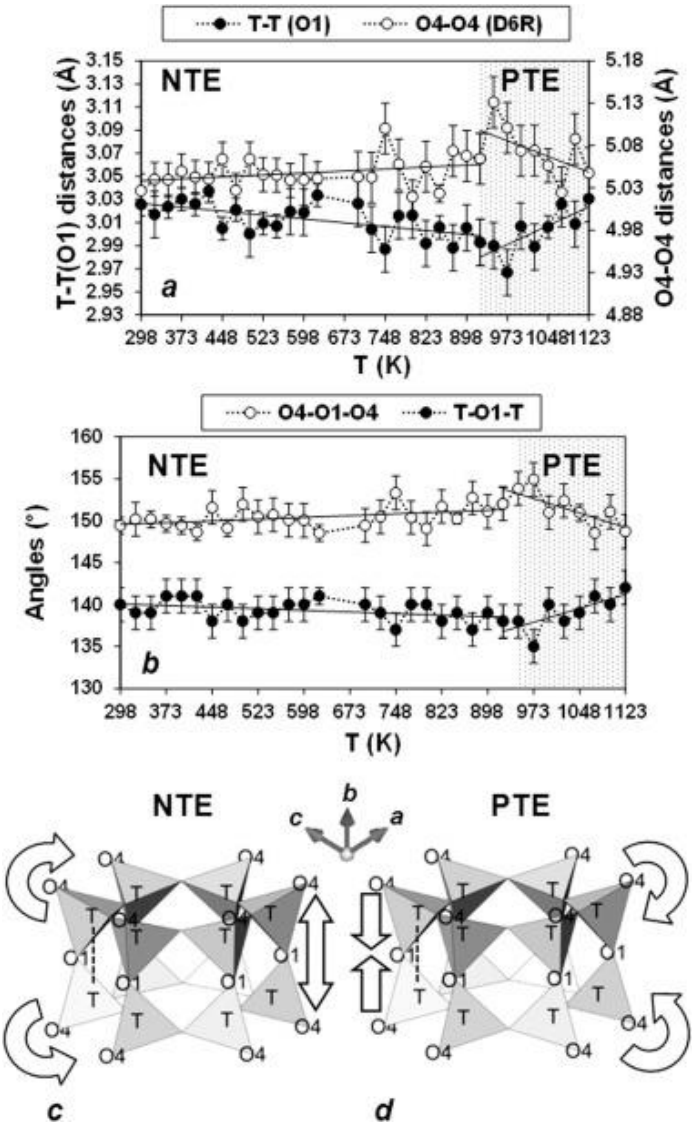

Fig. 6. Double-six ring (D6R) tetrahedral tilting and related variations in thickness. (a) T–T(O1) (full circles) and O4–O4 (empty circles) distances, and (b) T–O1–T (full circles) and O4–O1–O4 (empty circles) angles, as a function of temperature. The plot shows the two thermal behaviour regimes NTE and PTE. (c) and (d) D6R forming the faujasite framework; the arrows indicate the rotation modality followed by the tetrahedra during (c) NTE regime and (d) PTE regime, respectively.

It must be underlined that the deformation mechanism described immediately above for Si-Y is completely congruent with the mechanism largely accepted to describe T-induced deformations of zeolite frameworks, based on tetrahedral rotations around the 'hinges' and the consequent T–O–T angle distortions. In particular, all the zeolites characterized by the presence of D6Rs accommodate the effects of applied non-ambient conditions, by adjusting the geometry of this building unit [13], [44], [52], [53], [54], [55], [56] and [57].

The tetrahedral tilting of the D6R unit also induces variations in the geometry of the 6MRs and 12MRs. To describe the deformations undergone by the 6MRs, a ditrigonalization index ($I_{d\,\mathrm{D6R}}$ = O2–O2/O3–O3; $I_{d\,6\mathrm{R}}$ = O4–O4/O2–O2; Fig. 7a and b) was defined and reported as a function of T in Fig. 7c for the 6MRs involved in the D6R ($6\mathrm{MR}_{\mathrm{D6R}}$), and in Fig. 7d for the 6MRs of the sodalite cage ($6\mathrm{MR}_{\mathrm{sod}}$). The plots show that both the 6MRs become more hexagonal upon heating due to the effective decrease (i.e. beyond the error bar) of O3–O3 and O4–O4 distances (see Table 3). However, the regularization process of the $6\mathrm{MR}_{\mathrm{D6R}}$ in the PTE regime seems more marked compared to that of the $6\mathrm{MR}_{\mathrm{sod}}$ (Fig. 7). The geometrical variations of the

$6MR_{sod}$ are also accompanied by slight variations in its diameter (O2–O4, Table 3), which decreases in the NTE regime and slightly increases in the PTE regime, following the evolution of the unit-cell parameters.

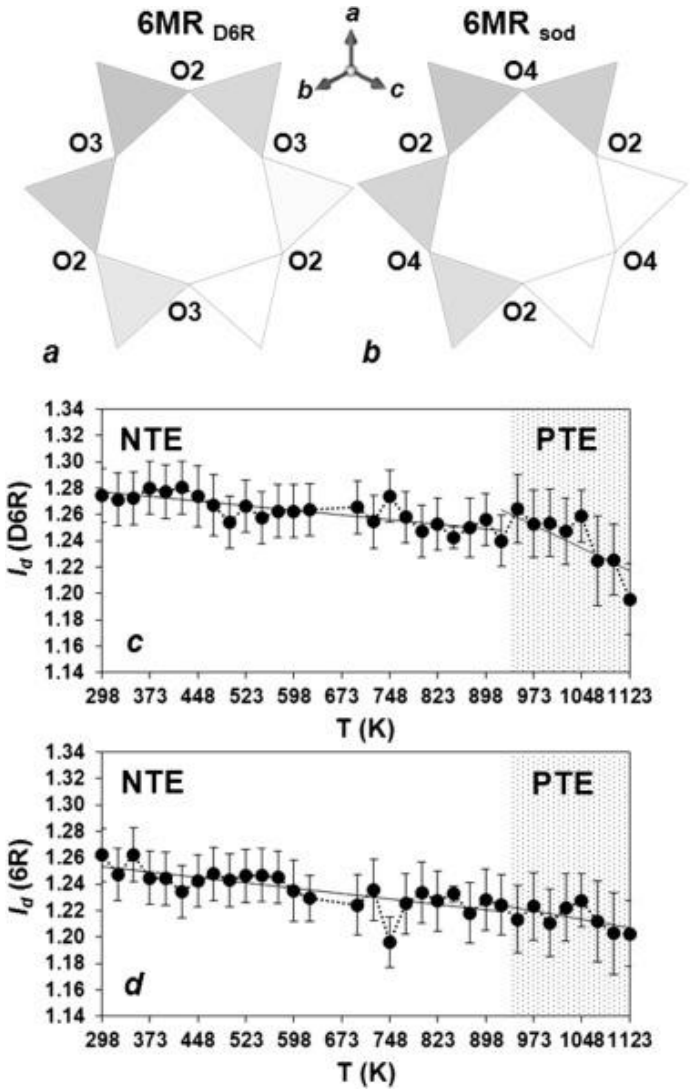

Fig. 7. 6-membered ring involved in the D6R ($6MR_{D6R}$) (a) and 6-membered ring of the sodalite cage ($6MR_{sod}$) (b). Ditrigonalization index of $6MR_{D6R}$ ($I_{d\,D6R}$) (c) and $6MR_{sod}$ ($I_{d\,6R}$) (d) as a function of temperature. The plot shows the two thermal behaviour regimes NTE and PTE.

The O1–O1 diameter of the 12MR aperture significantly decreases and increases in the NTE and PTE regimes, respectively (Table 3 and Fig. 8) as a consequence of the inversion of the D6R tilting. At the same time, no relevant variations are observed for the O4–O4 diameter in the NTE range, while a slight decrease is observed in the PTE range. As a result, the ellipticity (E, defined as the ratio between major and minor diameter, Table 3) increases in the NTE range and decreases in the PTE range.

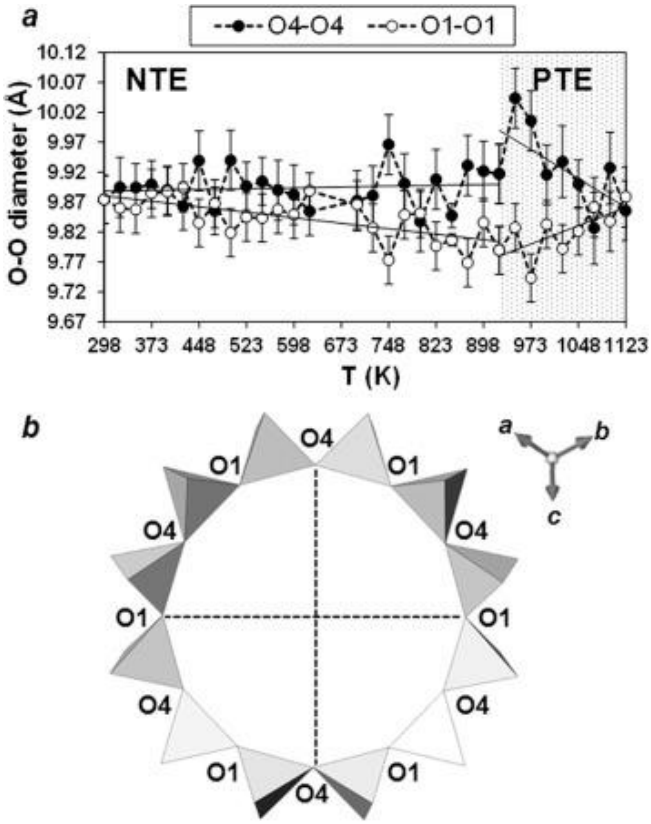

Fig. 8. (a) O1–O1 and O4–O4 diameters of the 12-membered ring (12MR) as a function of temperature. The plot shows the two thermal behaviour regimes NTE and PTE. (b) 12MR.

4. Comparative discussion

Table 4 was compiled with the aim of developing a comparative discussion between the present results and those reported in literature, which includes experimental data for several anhydrous porous materials exhibiting NTE behaviour. In particular, pure-silica phases are reported in bold, while the alumino-silicate materials containing extraframework cations are in *cursive*; the remaining samples are porous materials with framework substitutions and no or only minor presence of extraframework cations. It is worth noting that this discussion is not exhaustive and, most important, is rendered extremely difficult by the variability of the experimental conditions adopted in the various studies. When possible, and to facilitate comparison, Table 4 reports the linear and volume expansion coefficients determined for the samples, not only in the overall investigated T-range, but also in more restricted sub-ranges of the same experiment.

Table 4. Experimental data for selected anhydrous porous materials with NTE behaviour. Pure-silica phases are reported in bold, while the alumino-silicate materials containing extraframework cations are in italic; the remaining samples are porous materials with framework substitutions and no or minor presence of extraframework cations.

Sample	α_a (10^{-6} K^{-1})	α_b (10^{-6} K^{-1})	α_c (10^{-6} K^{-1})	α_V (10^{-6} K^{-1})	T-range (K)	Channel system	F.D. (Si) Atlas 2007	References
AEI ($AlPO_4$-18)	−11.94	−6.81	−7.32	−26.01	105–455	3	15.1	[34]
AFI ($AlPO_4$-5)	−5.1	−5.1	−3.7	−14.5	424–774	1	16.9	[14]
CHA (AlPO-34)	−9.27	−9.27	−5.54	−24.03	110–460	3	15.1	[34]
CHA (GaPO-34)	+2.15	+2.15	−20.30	−16.03	260–	3	15.1	[34]

Sample	α_a (10^{-6} K^{-1})	α_b (10^{-6} K^{-1})	α_c (10^{-6} K^{-1})	α_V (10^{-6} K^{-1})	T-range (K)	Channel system	F.D. (Si) Atlas 2007	References
					460			
CHA (Si-CHA)	−8.24	−8.24	−13.3	−28.5	293–873	3	15.1	[17]
CHA (Si-CHA)	−9.11	−9.11	−3.08	−21.22	308–753	3	15.1	[40]
DDR (deca-dodecasil 3R)	−2.8	−2.8	−3.1	−8.7	492–1185	2	17.9	[14]
DOH (dodecasil 1H)	−0.6	−0.6	−3.1	−3.1	573–996	0	17.0	[14]
ERI ($AlPO_4$-17)	−15.3	−15.3	−4.52	−35.1	18–300	3	16.1	[15]
ERI (MAPO-17)	−9.16	−9.16	+4.66	−4.6	323–773	3	16.1	[17]
FAU (Si-Y)	−4.0	−4.0	−4.0	−11.8	298–923	3	13.3	This work
FAU (Si-Y)	+10.0	+10.0	+10.0	+30.0	923–1123	3	13.3	This work
FAU (Si-Y)	−0.6	−0.6	−0.6	−1.7	298–1123	3	13.3	This work
FAU (Si-Y)	−4.6	−4.6	−4.6	−13.8	298–573	3	13.3	This work
FAU (Si-Y)	−4.6	−4.6	−4.6	−13.6	298–773	3	13.3	This work
FAU (Si-Y)	−4.2	−4.2	−4.2	−12.6	25–573	3	13.3	[16]
FAU (Na-X; Si/Al = 1.54)	−0.74	−0.74	−0.74	−2.21	25–293	3	13.3	[41]
FAU(SAPO-37)	−3.57	−3.57	−3.57	−10.7	303–773	3	13.3	[44]
FAU(SAPO-37)	−5.20	−5.20	−5.20	−15.6	303–373	3	13.3	[44]
FAU(SAPO-37)	−4.07	−4.07	−4.07	−12.2	303–573	3	13.3	[44]
FER	+8.1	−2.8	+16.1	+25.1	150–400	2	17.6	[19]
FER	−6.7	−7.1	−10.6	−24.2	420–560	2	17.6	[19]
IFR (ITQ-4)	−11.5	−7.47	+7.19	−9.1	95–510	1	17.2	[17]
ISV (ITQ-7)	−2.28	−2.28	−1.05	−5.6	473–873	2	15.0	[17]
ITE (ITQ-3)	−0.29	−2.06	−10.1	−11.4	323–823	2	15.7	[12]
LTA (ITQ-29 = Si-LTA)	−7.37	−7.37	−7.37	−22.1	100–300	3	14.2	[35]
LTA (Ag-A)	−2.56	−2.56	−2.56	−7.68	100–300	3	14.2	[35]
LTA (Na-A)	−2.11	−2.11	−2.11	−6.34	100–300	3	14.2	[36]
LTA (Rb0.79Na0.21-A)	−0.02	−0.02	−0.02	−0.78	100–300	3	14.2	[36]
LTA (Cs0.58Na0.42-A)	−0.59	−0.59	−0.59	−1.76	100–	3	14.2	[36]

Sample	α_a (10^{-6} K^{-1})	α_b (10^{-6} K^{-1})	α_c (10^{-6} K^{-1})	α_V (10^{-6} K^{-1})	T-range (K)	Channel system	F.D. (Si) Atlas 2007	References
					300			
MFI (Si-ZSM-5)	−5.5	−6.9	−2.8	−15.1	393–975	3	18.4	[14]
MFI (silicalite-1)	−5758	−0.485	−0.619	−6.75	298–1023	3	18.4	[26]
MFI (silicalite-1)				−7.49	373–773	3	18.4	[28]
MFI (H-ZSM-5; SiO_2/Al_2O_3 = 30)	−7.12	−6.81	−8.00	−18.66	793–953	3	18.4	[30]
MFI (H-ZSM-5; SiO_2/Al_2O_3 = 30)	−30.24	−21.67	−24.76	−77.25	953–1113	3	18.4	[30]
MFI ($Na_{4.6}[B_{9.3}Si_{86.7}O_{192}]$)	10.5	11.5	6.4	28.5	773–1003	3	18.4	[33]
MFI (Fe-silicalite-1; Si/Fe = 55)				−13.48	373–773	3	18.4	[28]
MFI (Fe-silicalite-1; Si/Fe = 50)	−2765	−4720	−5544	−12.91	298–1023	3	18.4	[26]
MFI (Ti-silicalite-1; Si/Ti = 50)	−7328	−3740	−5040	−16.02	298–1023	3	18.4	[26]
MFI (Zr-silicalite-1; Si/Zr = 50)	−8237	−4.50	−5251	−17.92	298–1023	3	18.4	[26]
MTN (dodecasil 3C)	−1.7	−1.7	−1.7	−5.0	463–1002	0	17.2	[14]
MWW (ITQ-1)	−4.23	−4.23	−3.21	−12.1	323–773	2	15.9	[12]
SOD (Si-SOD)	−4.7	−4.7	−4.7	−14.0	1033–1123	0	17.2	[40]
STF (ITQ-9)	−5.58	−2.37	−2.19	−10.0	293–873	1	16.9	[17]
STT (SSZ-23)	−6.09	−3.21	−0.73	−10.3	323–773	2	17.0	[12]

Firstly, the results obtained in this work for the thermal behaviour of Si-Y must be compared to those of Attfield and Sleight [16]. Considering the overall T-range in which the present sample undergoes NTE (298–923 K) and the previously investigated heating range (25–573 K [16]), the agreement between the two α_V values is very good (-11.77×10^{-6} K^{-1} and -12.6×10^{-6} K^{-1}, respectively). As regards only the T-range common to the two experiments (303–573 K), the following α_V values are obtained: -13.76×10^{-6} K^{-1} (this work), and -11.5×10^{-6} K^{-1}[16], showing a slightly higher negative expansion for the present sample in this heating region. This difference could be ascribed to the different experimental conditions adopted in the two experiments, which can strongly influence zeolite thermal behaviour [21]. Just to cite one of the influencing parameters Attfield and Sleight dehydrated their sample at 330 °C for 12 h under vacuum before performing the heating ramp in a sealed capillary.

The present results for Si-Y can also be compared to the thermal behaviour of SAPO-37 (the Si, Al, P counterpart of faujasite [44]), in the same 303–773 K T-range. Again in this case, the present sample exhibits a higher α_V value ($-13.6^{-6} \times 10^{-6}$ K^{-1}) compared to the SAPO counterpart (-10.7×10^{-6} K^{-1}, Table 4). This result disagrees with the conclusions reported by Buragadda et al. [44] that the substitution of Si by Al and P has essentially no effect on the thermal expansion properties of FAU-type materials. Several other literature

data sources reported in Table 4 instead indicate that the framework cation vicariance significantly affects NTE. For example, the thermal behaviour of MFI phases is strongly dependent on the substitution of B [33], Fe, Ti, or Zr for Si [27] and [28]; and similarly, the CHA structure-type materials Si-CHA, AlPO-34, and GaPO-34 have extremely different NTE coefficient values.

Previous studies on various siliceous and non-siliceous zeolites [17] and [22] suggested that high framework density and low channel system dimensionality favour PTE behaviour of porous phases. However, observing Table 4, this appears not to be true. Instead, several dense zeolites with zero- or one-dimensional channel system [AFI ($AlPO_4$-5), DOH (dodecasil 1H), IFR (ITQ-4), MTN (dodecasil 3C), SOD (Si-SOD), STF (ITQ-9)] exhibit NTE.

An analysis of Table 4 (and of the literature cited therein) also helps in estimating the crucial effect that the presence of extraframework cations in zeolite pores has on a material's thermal behaviour. For instance, Carey et al. [36] demonstrated that cation-induced strains play a fundamental role in the thermal behaviour mechanism of LTA-zeolites, inducing a thermal coefficient from negative to positive, depending on the monovalent cations present in the porosities. Specifically, ITQ-29 (the pure-Si phase with LTA topology), has the most negative α_V, its porosities being empty. A similar influence is also observed in FAU topology: Na-X with Si/Al = 1.54, and Na as counter-cation [42], shows a much lower NTE than the pure-Si counterpart studied here.

5. Conclusions

The results of this study make it possible to describe the T-induced effects on Si-Y structure over a much wider heating range than previously reported in literature. The most important new observations regard a structural interpretation of the change from an NTE to a PTE behaviour above 923 K. The structural factors driving this change, linked to the transverse and longitudinal T–O–T vibrations, are as follows:

i. the slope dependence of T–T(O1) distance and T–O1–T angle *vs.* T appreciably changes passing from the NTE to PTE regimes;
ii. the 6-membered rings become more hexagonal upon heating, but, for the 6-ring of the D6R, a clear slope change is observed passing from the NTE to PTE regimes;
iii. the 12MR aperture ellipticity increases with T in the NTE region, while it decreases in the PTE region.

An analysis of literature data regarding dehydrated zeolites with NTE behaviour leads to the conclusion that both the framework chemical composition and the extraframework content are crucial factors in determining the extent of NTE coefficients.

The conclusions of this work confirm the importance of accurate structural and compositional studies for understanding how to tune the thermal expansion of porous phases, in order to produce new materials of technological interest, like those characterized by very low or zero thermal expansion.

Acknowledgements

MCX beamline at Elettra is acknowledged for allocation of experimental beamtime. The authors are indebted Simona Bigi (Dipartimento di Scienze Chimiche e Geologiche, Università di Modena e Reggio Emilia) for thermogravimetric analyses. This work was supported by the Italian MIUR – PRIN2010-11 "Dalle materie prime del sistema Terra alle applicazioni tecnologiche: studi cristallochimici e strutturali' and FIRB, Futuro in Ricerca 'Impose Pressure and Change Technology' (RBFR12CLQD).

References

[1] C. Closmann, A.W. Sleight
J. Solid State Chem., 139 (1998), pp. 424–426

[2] N. Imanaka, M. Hiraiwa, G. Adachi, H. Dabkowska, A. Dabkowski
J. Cryst. Growth, 220 (2000), pp. 176–179

[3] A.W. Sleight
Curr. Opin. Solid State Mater., 3 (1998), pp. 128–131

[4] W. Miller, C.W. Smith, D.S. Mackenzie, K.E. Evans
J. Mater. Sci., 44 (2009), pp. 5441–5451

[5] C. Lind
Materials, 5 (2012), pp. 1125–1154

[6] C. Ernst, G. Broholm, R. Kowach, A.P. Ramirez
Nature, 396 (12) (1998), pp. 147–149

[7] K.D. Hammonds, A. Bosenick, M.T. Dove, V. Heine
Am. Mineral., 83 (1998), pp. 476–479

[8] T.A. Mary, J.S.O. Evans, T. Vogt, A.W. Sleight
Science, 272 (1996), pp. 90–92

[9] Y. Wu, A. Kobayashi, G.J. Halder, V.K. Peterson, K.W. Chapman, N. Lock, P.D. Southon, C.J. Kepert
Angew. Chem. Int. Ed., 47 (2008), pp. 8929–8932

[10] A.L. Goodwin, K.W. Chapman
J. Am. Chem. Soc., 127 (2005), pp. 17980–17981

[11] Y. Maniwa, R. Fujiwara, H. Kira, H. Tou, H. Kataura, S. Suzuki, Y. Achiba, E. Nishibori, M. Takata, M. Sakata, M. Fujiwara, H. Suematsu
Phys. Rev. B, 64 (2001), p. 241402(R)

[12] D.A. Woodcock, P. Lightfoot, P.A. Wright, L.A. Villaescusa, M.J. Diaz-Cabanas, M.A. Camblor
J. Mater. Chem., 9 (1999), pp. 349–351

[13] D.A. Woodcock, P. Lightfoot, L.A. Villaescusa, M.J. Diaz-Cabanas, M.A. Camblor, D. Engberg
Chem. Mater., 11 (1999), pp. 2508–2514

[14] S.H. Park, R.W. Grosse-Kunstleve, H. Graetsch, H. Gies
Stud. Surf. Sci. Catal., 105 (1997), pp. 1989–1994

[15] M.P. Attfield, A.W. Sleight
Chem. Mater., 10 (1998), pp. 2013–2019

[16] M.P. Attfield, A.W. Sleight
Chem. Commun. (1998), pp. 601–602

[17] P. Lightfoot, D.A. Woodcock, M.J. Maple, L.A. Villaescusa, P.A. Wright
J. Mater. Chem., 11 (2001), pp. 212–216

[18] L.A. Villaescusa, P. Lightfoot, S.J. Teat, R.E. Morris
J. Am. Chem. Soc., 123 (2001), pp. 5453–5459

[19] I. Bull, P. Lightfoot, L.A. Villaescusa, L.M. Bull, R.K. Gover, J.S. Evans, R.E. Morris
J. Am. Chem. Soc., 125 (2003), pp. 4342–4349

[20] V. Heine, P.R.L. Welche, M.T. Dove
J. Am. Chem. Soc., 82 (1999), pp. 1793–2595

[21] G. Cruciani
J. Phys. Chem. Solids, 67 (2006), pp. 1973–1994

[22] P. Tschaufeser, S.C. Parker
J. Phys. Chem., 99 (1995), pp. 10609–10615

[23] G. Cruciani, A. Gualtieri
Am. Mineral., 84 (1999), pp. 112–119

[24] C. Baerlocher, L.B. McCusker, D.H. Olson
Atlas of Zeolite Framework Types
(sixth ed.)Elsevier, Amsterdam (2007)

[25] P.M. Jardim, B.A. Marinkovic, A. Saavedra, L.Y. Lau, C. Baehtz, F. Rizzo
Microporous Mesoporous Mater., 76 (2004), pp. 23–28

[26] D.S. Bhange, V. Ramaswamy
Microporous Mesoporous Mater., 103 (2007), pp. 235–242

[27] D.S. Bhange, V. Ramaswamy
Mater. Res. Bull., 42 (2007), pp. 851–860

[28] D.S. Bhange, V. Ramaswamy
Microporous Mesoporous Mater., 130 (2010), pp. 322–326

[29] B.A. Marinkovic, P.M. Jardim, F. Rizzo, A. Saavedra, L.Y. Lau, E. Suard
Microporous Mesoporous Mater., 111 (2008), pp. 110–116

[30] B.A. Marinkovic, P.M. Jardim, A. Saavedra, L.Y. Lau, C. Baehtz, R.R. de Avillez, F. Rizzo
Microporous Mesoporous Mater., 71 (2004), pp. 117–124

[31] M. Noack, M. Schneider, A. Dittmar, G. Georgi, J. Caro
Microporous Mesoporous Mater., 117 (2009), pp. 10–21

[32] P.G. Krokidas, V. Nikolakis, V.N. Burganos
Microporous Mesoporous Mater., 155 (2012), pp. 65–70

[33] L. Leardini, A. Martucci, G. Cruciani
Microporous Mesoporous Mater., 173 (2013), pp. 6–14

[34] M. Amri, R.I. Walton
Chem. Mater., 21 (2009), pp. 3380–3390

[35] T. Carey, A. Corma, F. Rey, C.C. Tang, J.A. Hriljac, P.A. Anderson
Chem. Commun., 48 (2012), pp. 829–831

[36] T. Carey, C.C. Tang, J.A. Hriljac, P.A. Anderson
Chem. Mater., 26 (2014), pp. 1561–1566

[37] A. Bieniok, W.H. Baur
Acta Crystallogr., B49 (1993), pp. 817–822

[38] A. Bieniok, K.D. Hammonds
Microporous Mesoporous Mater., 25 (1998), pp. 193–200

[39] S.R.G. Balestra, J.J. Gutiérrez-Sevillano, P.J. Merkling, D. Dubbeldam, S. Calero
J. Phys. Chem. C, 117 (2013), pp. 11592–11599

[40] M.M. Martinez-Iñesta, R.F. Lobo

J. Phys. Chem. B, 109 (2005), pp. 9389–9396

[41] L. Leardini, A. Martucci, G. Cruciani
Microporous Mesoporous Mater., 151 (2012), pp. 163–171

[42] J.W. Couvest, R.H. Jones, S.C. Parker, P. Tschaufeser, C.R.A. Catlow
J. Phys.: Condens. Matter, 5 (1993), pp. L329–L332

[43] P.G. Krokidas, E.D. Skouras, V. Nikolakis, V.N. Burganos
J. Phys. Chem. C, 114 (2010), pp. 22441–22448

[44] V.R. Buragadda, L. Yu, F.G. Alabarse, A. Haidoux, C. Levelut, A. van der Lee, O. Cambon, J. Haines
RSC Adv., 3 (2013), pp. 9911–9915

[45] I. Braschi, S. Blasioli, L. Gigli, C.E. Gessa, A. Alberti, A. Martucci
J. Hazard. Mater., 17 (2010), pp. 218–225

[46] P. Riello, A. Lausi, J. Macleod, J. Rikkert Plaisier, G. Zerauschek, P. Fornasiero
J. Synchrotron Radiat., 20 (2013), pp. 194–196

[47] A.P. Hammersley, S.O. Svensson, A. Thomson
Nucl. Instrum. Methods Phys. Res. A, 346 (1994), pp. 312–321

[48] A.C. Larson, R.B. von Dreele, Report LAUR 86, 1994.

[49] B.H. Toby
J. Appl. Crystallogr., 34 (2001), pp. 210–213

[50] P. Thompson, D.E. Cox, J.B. Hastings
J. Appl. Crystallogr., 20 (1987), pp. 79–83

[51] R.T. Downs, G.V. Gibbs, K.L. Bartelmehs, M.B. Boisen Jr.
Am. Mineral., 77 (1992), pp. 751–757

[52] R. Arletti, G. Vezzalini, S. Quartieri, F. Cámara, M. Alvaro
Am. Mineral., 98 (2013), pp. 2063–2074

[53] M. Colligan, P.M. Forster, A.K. Cheetham, Y. Lee, T. Vogt, J.A. Hriljac
J. Am. Chem. Soc., 126 (2004), pp. 12015–12022

[54] M. Zema, S.C. Tarantino, G. Montagna
Chem. Mater., 20 (2008), pp. 5876–5887

[55] G.D. Gatta, P. Comodi, P.F. Zanazzi, T.B. Ballaran
Am. Mineral., 90 (2005), pp. 645–652

[56] L. Leardini, A. Martucci, A. Alberti, G. Cruciani
Microporous Mesoporous Mater., 167 (2013), pp. 117–126

[57] L. Leardini, S. Quartieri, G. Vezzalini, A. Martucci, V. Dmitriev
Microporous Mesoporous Mater., 170 (2013), pp. 52–61

[58] K. Momma, F. Izumi
J. Appl. Crystallogr., 44 (2011), pp. 1272–1276

Corresponding author at: Dipartimento di Scienze della Terra, Università di Messina, Viale Ferdinando Stagno d'Alcontres 31, I-98166 Messina, S. Agata, Italy. Tel.: +39 (0)90 6765096; fax: +39 (0)90 392333.